

# Elastic wave-mode separation for TTI media<sup>a</sup>

<sup>a</sup>Published in Geophysics, 76, no. 4, T65-T78, (2011)

*Jia Yan and Paul Sava*  
*Center for Wave Phenomena*  
*Colorado School of Mines<sup>1</sup>*

## ABSTRACT

Seismic waves propagate through the earth as a superposition of different wave-modes. Seismic imaging in areas characterized by complex geology requires techniques based on accurate reconstruction of the seismic wavefields. A crucial component of the methods in this category, collectively known as wave-equation migration, is the imaging condition which extracts information about the discontinuities of physical properties from the reconstructed wavefields at every location in space. Conventional acoustic migration techniques image a scalar wavefield representing the P wave-mode, in contrast with elastic migration techniques which image a vector wavefield representing both the P and S wave-modes. For elastic imaging, it is desirable that the reconstructed vector fields are decomposed in pure wave-modes, such that the imaging condition produces interpretable images, characterizing for example PP or PS reflectivity. In anisotropic media, wave-mode separation can be achieved by projection of the reconstructed vector fields on the polarization vectors characterizing various wave modes. For heterogeneous media, the polarization directions change with position, therefore wave-mode separation needs to be implemented using space-domain filters. For transversely isotropic media with a tilted symmetry axis (TTI), the polarization vectors depend on the elastic material parameters, including the tilt angles. Using these parameters, I separate the wave-modes by constructing nine filters corresponding to the nine Cartesian components of the three polarization directions at every grid point. Since the S polarization vectors in TI media are not defined in the singular directions, e.g. along the symmetry axes, I construct these vectors by exploiting the orthogonality between the SV and SH polarization vectors, as well as their orthogonality with the P polarization vector. This procedure allows one to separate S wave-modes which are only kinematically correct. Realistic synthetic examples show that this wave-mode separation is effective for both 2D and 3D models with high heterogeneity and strong anisotropy.

<sup>1</sup>e-mail: [jyan@mines.edu](mailto:jyan@mines.edu), [psava@mines.edu](mailto:psava@mines.edu)

## INTRODUCTION

Although acoustic migration is currently the most common seismic imaging procedure, elastic imaging, with the addition of converted-waves, has been recognized to have potential advantages in seeing through gas-charged sediments and in structural and near surface imaging (Stewart et al., 2003). Two options are available for elastic imaging: 1) one can separate wave-modes at the surface and image with the separated PP and PS data using acoustic migration tools (Sun et al., 2004), or 2) one can extrapolate the recorded multicomponent data and image with the reconstructed elastic wavefields by applying an imaging condition to wave-modes separated in the vicinity of the image points (Yan and Sava, 2008). The first approach benefits from the simplicity of imaging with scalar waves, but it is based on the assumption that P and S modes can be successfully separated on the recording surface, which is difficult for complicated datasets. The second approach reconstructs elastic wavefields in the subsurface, thus capturing all possible wave-mode transmissions and reflections, although it increases the computational cost in elastic wavefields modeling. In addition, the elastic migration technique requires wave-mode separation before the application of an imaging condition to avoid crosstalk between different wave-modes.

In isotropic media, the P- and S-modes (shear waves do not split in isotropic media) can easily be separated by taking the divergence and curl of the elastic wavefield (Aki and Richards, 2002), and the procedure is effective in homogeneous as well as heterogeneous media. This is because, in the far field, P- and S-waves are polarized parallel and perpendicular to the wave vectors, respectively. The polarization directions of the P- and S-waves only depend on the wave propagation direction and are not altered by the medium. Therefore, the wave-mode separators are invariant with space, and divergence and curl can always be used to separate compressional (scalar) and shear (vector) wave-modes.

However, divergence and curl do not fully separate wave-modes in anisotropic media, because P- and S-waves are not polarized parallel and perpendicular to the wave vectors. Dellinger and Etgen (1990) separate wave-modes in homogeneous VTI (vertically transversely isotropic) media by projecting the vector wavefields onto the polarization vectors of each mode. In VTI media, the polarization vectors of P- and SV-waves depend on the anisotropy parameters  $\epsilon$  and  $\delta$  (Thomsen, 1986) and are spatially-varying when the medium is inhomogeneous. Therefore, Yan and Sava (2009) separate wave-modes in heterogeneous VTI media by filtering the wavefields with spatially varying separators in the space domain and show that separation is effective even for complex geology with high heterogeneity.

However, VTI models are suitable only for limited geological settings with horizontal layering. Many case studies have shown that TTI (tilted transversely isotropic) models better represent complex geologies like thrusts and fold belts, e.g., the Canadian Foothills (Godfrey, 1991). Using the VTI assumption to image structures characterized by TTI anisotropy introduces both kinematic and dynamical errors in migrated images. For example, Vestrum et al. (1999) and Isaac and Lawyer (1999) show

that seismic structures can be mispositioned if isotropy, or even VTI anisotropy, is assumed when the medium above the imaging targets is TTI. To carry out elastic wave-equation migration for TTI models and apply the imaging condition that cross-correlates the separated wave-modes, the wave-mode separation algorithm needs to be adapted to TTI media. For sedimentary layers bent under geological forces, TTI migration models usually incorporate locally varying tilts, and the local symmetry axes are assumed to be orthogonal to the reflectors throughout the model (C. et al., 2008; Alkhalifah and Sava, 2010). Therefore, in complex TI models, both the local anisotropy parameters  $\epsilon$  and  $\delta$ , and the local symmetry axes with tilt  $\nu$  and azimuth  $\alpha$  can be space-dependent.

This technique of separation by projecting the vector wavefields onto polarization vectors has been applied only to 2D VTI models (Dellinger, 1991; Yan and Sava, 2009) and for P-mode separation for 3D VTI models (Dellinger, 1991). For 3D models, the main challenge resides in the fact that fast and slow shear modes have non-linear polarizations along symmetry-axis propagation directions. It is possible to apply the 2D separation method to 3D TTI models using the following procedure. First, project the elastic wavefields onto symmetry planes (which contains P- and SV-modes) and their orthogonal directions (which contain the SH-mode only); then separate P- and SV-modes in the symmetry planes using divergence and curl operators for isotropic media or polarization vector projection for TI media. However, this approach is difficult as wavefields are usually constructed in Cartesian coordinates and symmetry planes of the models do not align with the Cartesian coordinates. Furthermore, for heterogeneous models, the symmetry planes change spatially, which makes projection of wavefields onto symmetry planes impossible. To avoid these problems, I propose a simpler and more straightforward solution to separate wave-modes with 3D operators, which eliminates the need for projecting the wavefields onto symmetry planes. The new approach constructs shear-wave filters by exploiting the mutual orthogonality of shear modes with the P mode, whose polarization vectors are computed by solving 3D Christoffel equations.

In this chapter, I briefly review wave-mode separation for 2D VTI media and then I extend the algorithm to symmetry planes of TTI media. Then, I generalize the wave-mode separation to 3D TI media. Finally, I demonstrate wave-mode separation in 2D with homogeneous and heterogeneous examples and separation in 3D with a homogeneous TTI example.

## WAVE-MODE SEPARATION FOR 2D TI MEDIA

### Wave-mode separation for symmetry planes of VTI media

Dellinger and Etgen (1990) separate *quasi*-P and *quasi*-SV modes in 2D VTI media by projecting the wavefields onto the directions in which P and S modes are polarized. For example, in the wavenumber domain, one can project the wavefields onto the

P-wave polarization vectors  $W_P$  to obtain *quasi*-P ( $qP$ ) waves:

$$\widetilde{qP} = i W_P(\mathbf{k}) \cdot \widetilde{\mathbf{W}} = i U_x \widetilde{W}_x + i U_z \widetilde{W}_z, \quad (1)$$

where  $\widetilde{qP}$  is the P-wave mode in the wavenumber domain,  $\mathbf{k} = \{k_x, k_z\}$  is the wavenumber vector,  $\widetilde{\mathbf{W}}$  is the elastic wavefield in the wavenumber domain, and  $W_P(\mathbf{k})$  is the P-wave polarization vector as a function of the wavenumber  $\mathbf{k}$ .

The polarization vectors  $W(\mathbf{k})$  of plane waves for VTI media in the symmetry planes can be found by solving the Christoffel equation (Aki and Richards, 2002; Tsvankin, 2005):

$$[\mathbf{G} - \rho V^2 \mathbf{I}] W = 0, \quad (2)$$

where  $\mathbf{G}$  is the Christoffel matrix with  $G_{ij} = c_{ijkl} n_j n_l$ , in which  $c_{ijkl}$  is the stiffness tensor. The vector  $\mathbf{n} = \frac{\mathbf{k}}{|\mathbf{k}|}$  is the unit vector orthogonal to the plane wavefront, with  $n_j$  and  $n_l$  being the components in the  $j$  and  $l$  directions,  $i, j, k, l = 1, 2, 3$ . The eigenvalues  $V$  of this system correspond to the phase velocities of different wave-modes and are dependent on the plane wave propagation direction  $\mathbf{k}$ .

For plane waves in the vertical symmetry plane of a TTI medium, since  $qP$  and  $qSV$  modes are decoupled from the SH-mode and polarized in the symmetry planes, one can set  $n_y = 0$  and obtain

$$\begin{bmatrix} G_{11} - \rho V^2 & G_{12} \\ G_{12} & G_{22} - \rho V^2 \end{bmatrix} \begin{bmatrix} U_x \\ U_z \end{bmatrix} = 0, \quad (3)$$

where

$$G_{11} = c_{11} n_x^2 + c_{55} n_z^2, \quad (4)$$

$$G_{12} = (c_{13} + c_{55}) n_x n_z, \quad (5)$$

$$G_{22} = c_{55} n_x^2 + c_{33} n_z^2. \quad (6)$$

Equation 3 allows one to compute the polarization vectors  $W_P = \{U_x, U_z\}$  and  $W_{SV} = \{-U_z, U_x\}$  (the eigenvectors of the matrix  $\mathbf{G}$ ) given the stiffness tensor at every location of the medium.

Equation 1 represents the separation process for the P-mode in 2D homogeneous VTI media. To separate wave-modes for heterogeneous models, one needs to use different polarization vectors at every location of the model (Yan and Sava, 2009), because the polarization vectors change spatially with medium parameters. In the space domain, an expression equivalent to equation 1 at each grid point is

$$qP = \nabla_a \cdot \mathbf{W} = L_x[W_x] + L_z[W_z], \quad (7)$$

where  $L[\cdot]$  indicates spatial filtering, and  $L_x$  and  $L_z$  are the filters to separate P waves representing the inverse Fourier transforms of  $i U_x$  and  $i U_z$ , respectively. The terms  $L_x$  and  $L_z$  define the ‘‘pseudo-derivative operators’’ in the  $x$  and  $z$  directions for a VTI medium, respectively, and they change according to the material parameters,  $V_{P0}$ ,  $V_{S0}$  ( $V_{P0}$  and  $V_{S0}$  are the P and S velocities along the symmetry axis, respectively),  $\epsilon$ , and  $\delta$  (Thomsen, 1986).

## Wave-mode separation for symmetry planes of TTI media

My separation algorithm for TTI models is similar to the approach used for VTI models. The main difference is that for VTI media, the wavefields consist of P- and SV-modes, and equations 1 and 7 can be used for separation in all vertical planes of a VTI medium. However, for TTI media, this separation only works in the plane containing the dip of the reflector, where P- and SV-waves are polarized, while other vertical planes contain SH-waves as well.

To obtain the polarization vectors for P and S modes in the symmetry planes of TTI media, one needs to solve for the Christoffel equation 3 with

$$G_{11} = c_{11}n_x^2 + 2c_{15}n_xn_z + c_{55}n_z^2, \quad (8)$$

$$G_{12} = c_{15}n_x^2 + (c_{13} + c_{55})n_xn_z + c_{35}n_z^2, \quad (9)$$

$$G_{22} = c_{55}n_x^2 + 2c_{35}n_xn_z + c_{33}n_z^2. \quad (10)$$

Here, since the symmetry axis of the TTI medium does not align with the vertical axis  $k_z$ , the TTI Christoffel matrix is different from its VTI equivalent. The stiffness tensor is determined by the parameters  $V_{P0}$ ,  $V_{S0}$ ,  $\epsilon$ ,  $\delta$ , and the tilt angle  $\nu$ .

In anisotropic media,  $W_P$  generally deviates from the wave vector direction  $\mathbf{k} = \frac{\omega}{V}\mathbf{n}$ , where  $\omega$  is the angular frequency,  $V$  is the phase vector. Figures 1(a) and (b) show the P-mode polarization in the wavenumber domain for a VTI medium and a TTI medium with a  $30^\circ$  tilt angle, respectively. The polarization vectors for the VTI medium deviate from radial directions, which represent the isotropic polarization vectors  $\mathbf{k}$ . The polarization vectors of the TTI medium are rotated  $30^\circ$  about the origin from the vectors of the VTI medium.

Figures ?? and ?? show the components of the P-wave polarization of a VTI medium and a TTI medium with a  $30^\circ$  tilt angle, respectively. Figure ?? shows that the polarization vectors in Figure ?? rotated to the symmetry axis and its orthogonal direction of the TTI medium. Comparing Figures ?? and ??, we see that within the circle of radius  $\pi$  radians, the components of this TTI medium are rotated  $30^\circ$  from those of the VTI medium. However, note that the  $z$  and  $x$  components of the polarization vectors for the VTI medium (Figure ??) are symmetric with respect to the  $x$  and  $z$  axes, respectively; in contrast, the vectors of the TTI medium (Figure ??) are not symmetric because of the non-alignment of the TTI symmetry with the Cartesian coordinates.

To maintain continuity at the negative and positive Nyquist wavenumbers for Fourier transform to obtain space-domain filters, i.e. at  $k_x, k_z = \pm\pi$  radians, one needs to apply tapers to the vector components. For VTI media, a taper corresponding to the function (Yan and Sava, 2009)

$$f(k) = -\frac{8 \sin(k)}{5k} + \frac{2 \sin(2k)}{5k} - \frac{8 \sin(3k)}{105k} + \frac{\sin(4k)}{140k} \quad (11)$$

can be applied to the  $x$  and  $z$  components of the polarization vectors (Figure ??), where  $k$  represent the components  $k_x$  and  $k_z$  of the vector  $\mathbf{k}$ . This taper ensures that

$U_x$  and  $U_z$  are zero at  $k_z = \pm\pi$  radians and  $k_x = \pm\pi$  radians, respectively. The components  $U_x$  and  $U_z$  are continuous in the  $z$  and  $x$  directions across the Nyquist wave numbers, respectively, due to the symmetry of the VTI media. Moreover, the application of this taper transforms polarization vector components to 8<sup>th</sup> order derivatives. If the components of the isotropic polarization vectors  $\mathbf{k}$  are tapered by the function in equation 11 and then transformed to the space domain, one obtains the conventional 8<sup>th</sup> order finite difference derivative operators  $\frac{\partial}{\partial x}$  and  $\frac{\partial}{\partial z}$  (Yan and Sava, 2009). Therefore, the VTI separators reduce to conventional derivatives—the components of the divergence and curl operators—when the medium is isotropic.

For TTI media, due to the asymmetry of the Fourier domain derivatives (Figure ??), one needs to apply a rotational symmetric taper to the polarization vector components to obtain continuity across Nyquist wavenumbers. A simple Gaussian taper

$$g(\mathbf{k}) = C \exp \left[ -\frac{|\mathbf{k}|^2}{2\sigma^2} \right] \quad (12)$$

can be used, where  $C$  is a normalizing constant. When one chooses a standard deviation of  $\sigma = 1$  radian, the magnitude of this taper at  $|\mathbf{k}| = \pi$  radians is about 0.7% of the peak value, and therefore the TTI components can be safely assumed to be continuous across the Nyquist wavenumbers. Tapering the polarization vector components in Figure 2 with the function in equation 12, one obtains the plots in Figure 3. The panels in Figure 3, which exhibits circular continuity across the Nyquist wavenumbers, transform to the space-domain separators in Figure 4. The space-domain filters for TTI media is rotated from the VTI filters, also by the tilt angle  $\nu$ .

The value of  $\sigma$  determines the size of the operators in the space domain and also affects the frequency content of the separated wave-modes. For example, Figure 5 shows the component  $U_z$  and operator  $L_z$  for  $\sigma$  values of 0.25, 1.00, and 1.25 radians. A larger value of  $\sigma$  results in more concentrated operators in the space domain and better preserved frequency of the separated wave-modes. However, one needs to ensure that the function  $g(\mathbf{k})$  at  $|\mathbf{k}| = \pi$  radians is small enough to assume continuity of the value function across Nyquist wavenumbers. When one chooses  $\sigma = 1$  radian, the TTI components can be safely assumed to be continuous across the Nyquist wavenumbers.

For heterogeneous models, I can pre-compute the polarization vectors at each grid point as a function of the  $V_{P0}/V_{S0}$  ratio, the Thomsen parameters  $\epsilon$  and  $\delta$ , and tilt angle  $\nu$ . I then transform the tapered polarization vector components to the space domain to obtain the spatially-varying separators  $L_x$  and  $L_z$ . The separators for the entire model are stored and used to separate P- and S-modes from reconstructed elastic wavefields at different time steps. Thus, wavefield separation in TI media can be achieved simply by non-stationary filtering with spatially varying operators. I assume that the medium parameters vary slowly in space and that they are locally homogeneous. For complex media, the localized operators behave similarly to the

long finite difference operators used for finite difference modeling at locations where medium parameters change rapidly.

## WAVE-MODE SEPARATION FOR 3D TI MEDIA

In order to separate all three modes—P, SV, and SH—in a 3D TI medium, one needs to construct 3D separators. Dellinger (1991) shows that P-waves can be separated from two shear modes by a straightforward extension of the 2D algorithm. Indeed, for 3D TI media, one can always obtain the P-mode by constructing P-wave separators represented by the polarization vector  $W_P = \{U_x, U_y, U_z\}$  and then projecting the 3D elastic wavefields onto the vector  $W_P$ . The P-wave polarization vector with components  $\{U_x, U_y, U_z\}$  is obtained by solving the 3D Christoffel matrix (Aki and Richards, 2002; Tsvankin, 2005):

$$\begin{bmatrix} G_{11} - \rho V^2 & G_{12} & G_{13} \\ G_{12} & G_{22} - \rho V^2 & G_{23} \\ G_{13} & G_{23} & G_{33} - \rho V^2 \end{bmatrix} \begin{bmatrix} U_x \\ U_y \\ U_z \end{bmatrix} = 0. \quad (13)$$

The notations in this equation have the same definitions as in equation 2. For TTI media, the matrix  $\mathbf{G}$  has the elements

$$G_{11} = c_{11}n_x^2 + c_{66}n_y^2 + c_{55}n_z^2 + 2c_{16}n_xn_y + 2c_{15}n_xn_z + 2c_{56}n_yn_z, \quad (14)$$

$$G_{22} = c_{66}n_x^2 + c_{22}n_y^2 + c_{44}n_z^2 + 2c_{26}n_xn_y + (c_{45} + c_{46})n_xn_z + 2c_{24}n_yn_z, \quad (15)$$

$$G_{33} = c_{55}n_x^2 + c_{44}n_y^2 + c_{33}n_z^2 + 2c_{45}n_xn_y + 2c_{35}n_xn_z + 2c_{34}n_yn_z, \quad (16)$$

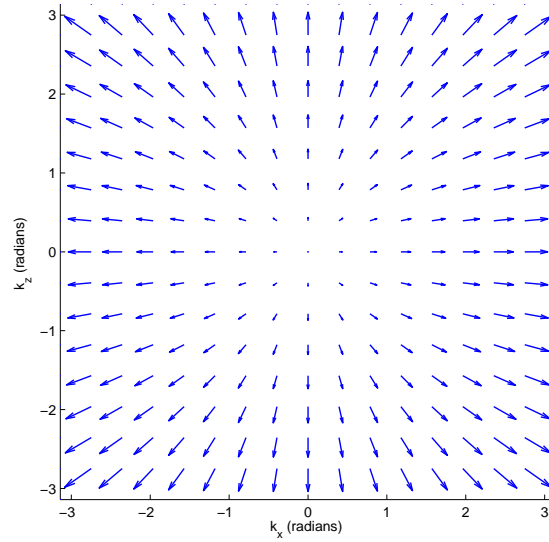
$$G_{12} = c_{16}n_x^2 + c_{26}n_y^2 + c_{45}n_z^2 + (c_{12} + c_{66})n_xn_y + (c_{14} + c_{56})n_xn_z + (c_{25} + c_{46})n_yn_z, \quad (17)$$

$$G_{13} = c_{15}n_x^2 + c_{46}n_y^2 + c_{35}n_z^2 + (c_{14} + c_{56})n_xn_y + (c_{13} + c_{55})n_xn_z + (c_{36} + c_{45})n_yn_z, \quad (18)$$

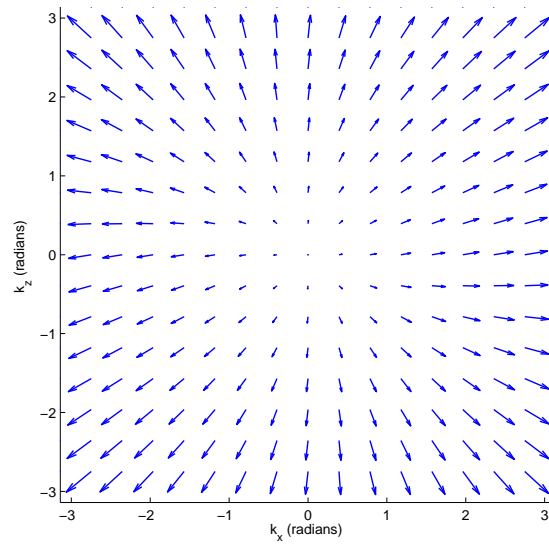
$$G_{23} = c_{56}n_x^2 + c_{24}n_y^2 + c_{34}n_z^2 + (c_{25} + c_{46})n_xn_y + (c_{36} + c_{45})n_xn_z + (c_{23} + c_{44})n_yn_z. \quad (19)$$

When constructing shear mode separators, one faces an additional complication: SV- and SH-waves have the same velocity along the symmetry axis of a 3D TI medium, and this singularity prevents one from obtaining polarization vectors for shear modes in this particular direction by solving the Christoffel equation (Tsvankin, 2005). In 3D TI media, the polarization of the shear modes around the singular directions are non-linear and cannot be characterized by a plane-wave solution. Consequently, constructing 3D global separators for fast and slow shear modes is difficult.

To mitigate the effects of the shear wave-mode singularity, I use the mutual orthogonality among the P, SV, and SH modes depicted in Figure 6. In this figure, vector  $\mathbf{n} = \{\sin \nu \cos \alpha, \sin \nu \sin \alpha, \cos \nu\}$  represents the symmetry axis of a TTI medium, with  $\nu$  and  $\alpha$  being the tilt and azimuth of the symmetry axis, respectively. The



(a)



(b)

Figure 1: The polarization vectors of P-mode as a function of normalized wavenumbers  $k_x$  and  $k_z$  ranging from  $-\pi$  radians to  $+\pi$  radians, for (a) a VTI model with  $V_{P0} = 3.0$  km/s,  $V_{S0} = 1.5$  km/s,  $\epsilon = 0.25$  and  $\delta = -0.29$ , and for (b) a TTI model with the same model parameters as (a) and a symmetry axis tilt  $\nu = 30^\circ$ . The vectors in (b) are rotated  $30^\circ$  with respect to the vectors in (a) around  $k_x = 0$  and  $k_z = 0$ .

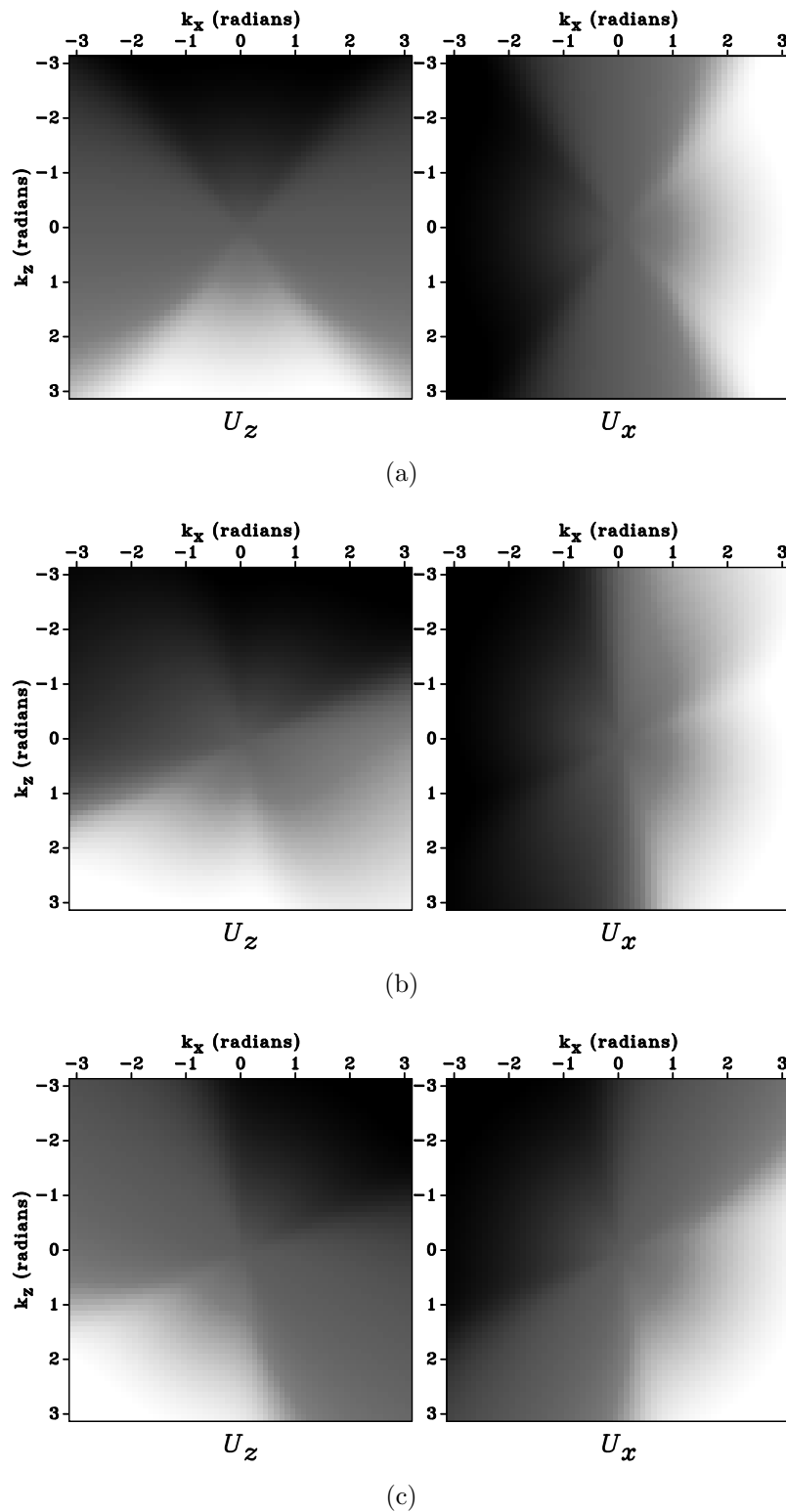


Figure 2: The  $z$  and  $x$  components of the polarization vectors for P-mode in the Fourier domain for (a) a VTI medium with  $\epsilon = 0.25$  and  $\delta = -0.29$ , and for (b) a TTI medium with  $\epsilon = 0.25$ ,  $\delta = -0.29$ , and  $\nu = 30^\circ$ . Panel (c) represents the projection of the polarization vectors shown in (b) onto the tilt axis and its orthogonal direction.

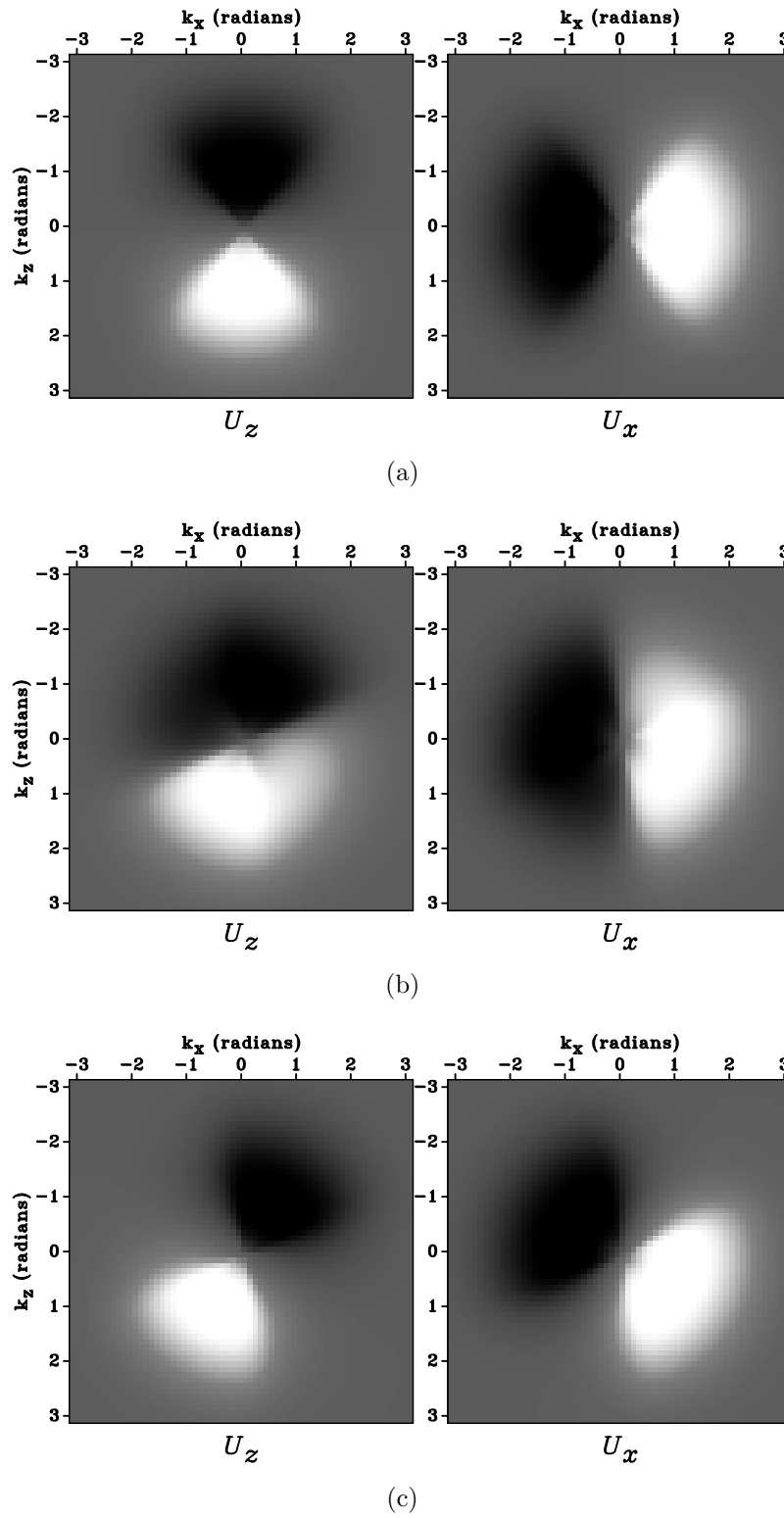


Figure 3: The wavenumber-domain vectors in Figure 2 are tapered by the function in equation 12 to avoid Nyquist discontinuity. Panel (a) corresponds to Figure 2(a), panel (b) corresponds to Figure 2(b), and panel (c) corresponds to Figure 2(c).

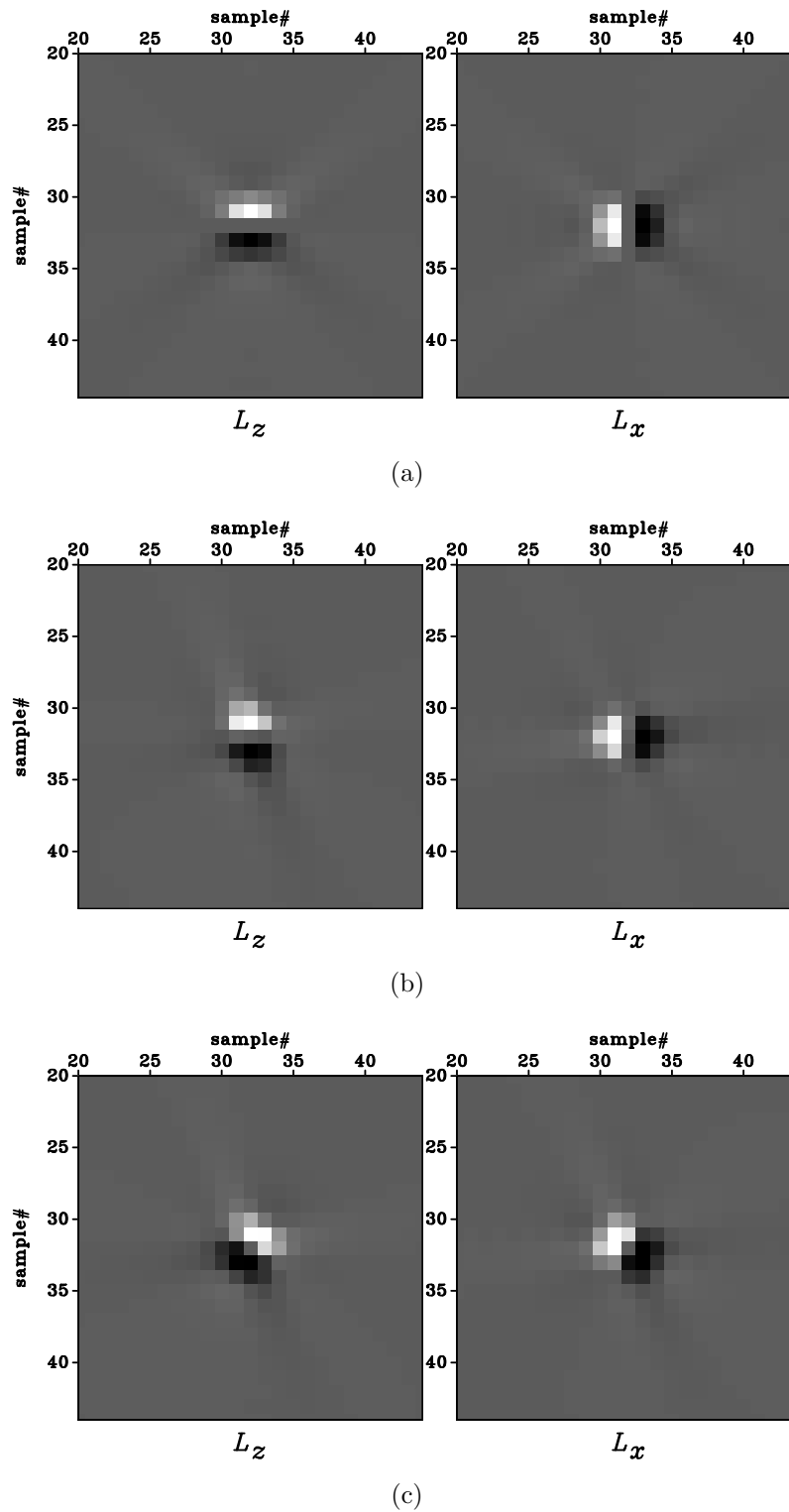
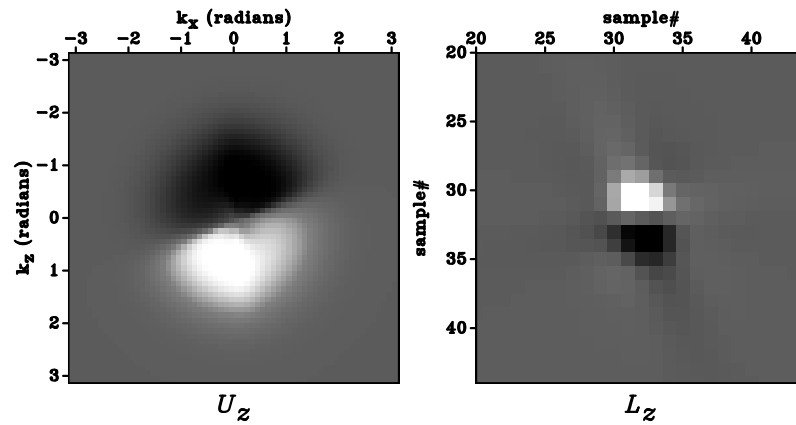
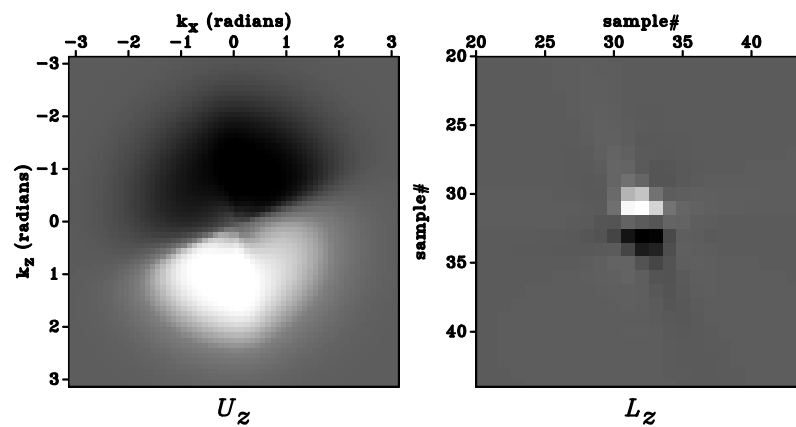


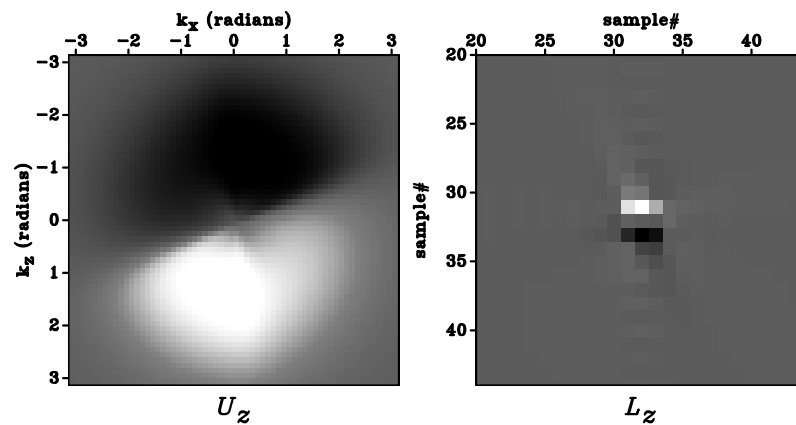
Figure 4: The space-domain wave-mode separators for the medium shown in Figure 1. They are the Fourier transformation of the polarization vectors shown in Figure 3. Panel (a) corresponds to Figure 3(a), panel (b) corresponds to Figure 3(b), and panel (c) corresponds to Figure 3(c). The zoomed views show  $24 \times 24$  samples out of the original  $64 \times 64$  samples around the center of the filters.



(a)



(b)



(c)

Figure 5: Panels (a)–(c) correspond to component  $U_z$  (left) and operator  $L_z$  (right) for  $\sigma$  values of 0.25, 1.00, and 1.25 radians in equation 12, respectively. A larger value of  $\sigma$  results in more spread components in the wavenumber domain and more concentrated operators in the space domain.

wave vector  $\mathbf{k}$  characterizes the propagation direction of a plane wave. Vectors  $\mathbf{P}$ ,  $\mathbf{SV}$ , and  $\mathbf{SH}$  symbolize the compressional, and fast and slow shear polarization directions, respectively. For TI media, plane waves propagate in symmetry planes, and the symmetry axis  $\mathbf{n}$  and any wave vector  $\mathbf{k}$  form a symmetry plane. For a plane wave propagating in the direction  $\mathbf{k}$ , the P-wave is polarized in this symmetry plane and deviates from the vector  $\mathbf{k}$ ; the SV- and SH-waves are polarized perpendicular to the P-mode, in and out of the symmetry plane, respectively.

Using this mutual orthogonality among all three modes, I first obtain the SH-wave polarization vector  $W_{SH}$  by cross multiplying vectors  $\mathbf{n}$  and  $\mathbf{k}$ , which ensures that the SH mode is polarized orthogonal to symmetry planes:

$$\begin{aligned} W_{SH} &= \mathbf{n} \times \mathbf{k} \\ &= \{k_z n_y - k_y n_z, \\ &\quad k_x n_z - k_z n_x, \\ &\quad k_y n_x - k_x n_y\}. \end{aligned} \quad (20)$$

Then I calculate the SV polarization vector  $W_{SV}$  by cross multiplying polarization vectors P and SH modes, which ensures the orthogonality between SV and P modes and SV and SH modes:

$$\begin{aligned} W_{SV} &= W_P \times W_{SH}, \\ &= \{k_y n_x U_y - k_x n_y U_y + k_z n_x U_z - k_x n_z U_z, \\ &\quad k_z n_y U_z - k_y n_z U_z + k_x n_y U_x - k_y n_x U_x, \\ &\quad k_x n_z U_x - k_z n_x U_x + k_y n_z U_y - k_z n_y U_y\}. \end{aligned} \quad (21)$$

Here, the magnitude of the P-wave polarization vectors for a certain wavenumber  $|\mathbf{k}|$  is a constant:

$$|U_P| = \sqrt{U_x^2 + U_y^2 + U_z^2} = c. \quad (22)$$

This ensures that for a certain wavenumber, P-waves obtained by projecting the elastic wavefields onto the polarization vectors are uniformly scaled. For comparison, the magnitudes of all three modes are respectively

$$|U_P| = c, \quad (23)$$

$$|U_{SV}| = c \sin \phi, \quad (24)$$

$$|U_{SH}| = c \sin \phi, \quad (25)$$

where  $\phi$  is the polar angle of the propagating plane wave, i.e., the angle between vectors  $\mathbf{k}$  and  $\mathbf{n}$ . Figure 7 shows the polarization vectors of P-, SH-, and SV-modes computed using equations 13, 20, and 21, respectively. The P-wave polarization vectors in Figure 7(a) all have the same magnitude, but the SV and SH polarization vectors in Figures 7(c) and (b) vary in magnitude. In the symmetry axis direction, they become zero. The zero amplitude of the shear modes in the symmetry axis direction is not an abrupt but a continuous change over nearby propagation angles.

Using separators represented by solutions to equation 13 and expressions 20 and 21 to filter the wavefields, I obtain separated shear modes that are scaled differently than the P-mode. For a certain wavenumber, the shear modes are scaled by  $\sin \phi$ , with  $\phi$  being the polar angle, which increases from zero in the symmetry axis to unity in the orthogonal propagation directions. Therefore, the separated SV- and SH-waves have zero amplitude in the symmetry axis direction, and the amplitudes of the shear modes are just kinematically correct.

The components of the polarization vectors for P-, SV-, and SH-waves can be transformed back to the space domain to construct spatial filters for 3D heterogeneous TI media. For example, Figure 8 illustrates nine spatial filters transformed from the Cartesian components of the polarization vectors shown in Figure 7. All these filters can be spatially varying when the medium is heterogeneous. Therefore, in principle, wave-mode separation in 3D would perform well even for models that have complex structures and arbitrary tilts and azimuths of TI symmetry.

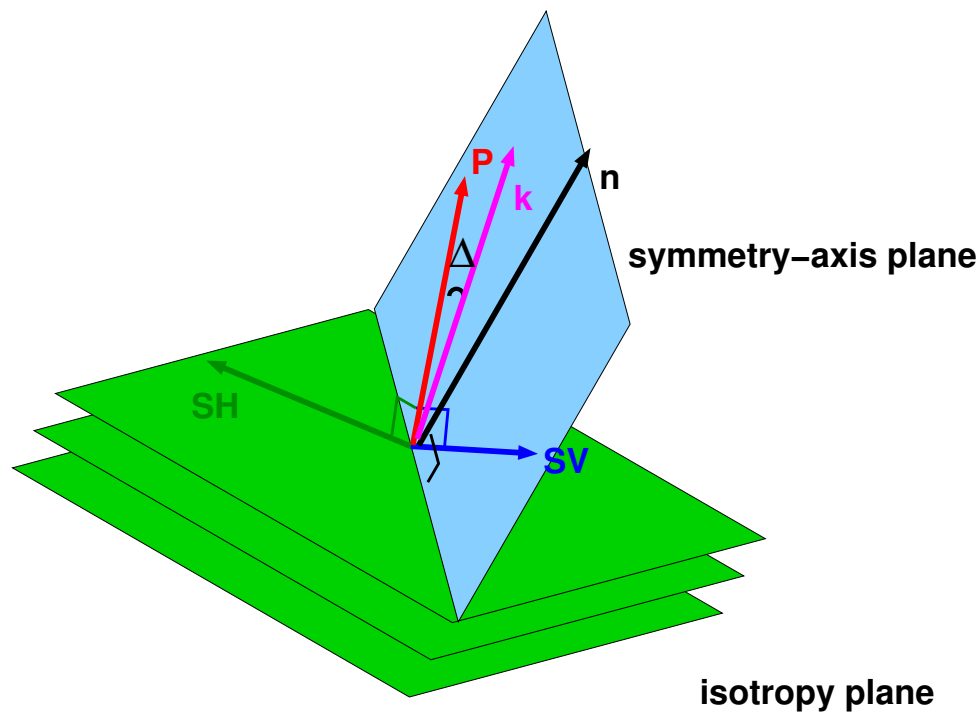


Figure 6: A schematic showing the elastic wave-modes polarization in a 3D TI medium. The three parallel planes represent the isotropy planes of the medium. The vector  $\mathbf{n}$  represents the symmetry axis, which is orthogonal to the isotropy plane. The vector  $\mathbf{k}$  is the propagation direction of a plane wave. The wave-modes P, SV, and SH are polarized in the direction  $\mathbf{P}$ ,  $\mathbf{SV}$ , and  $\mathbf{SH}$ , respectively. The three modes are polarized orthogonal to each other.

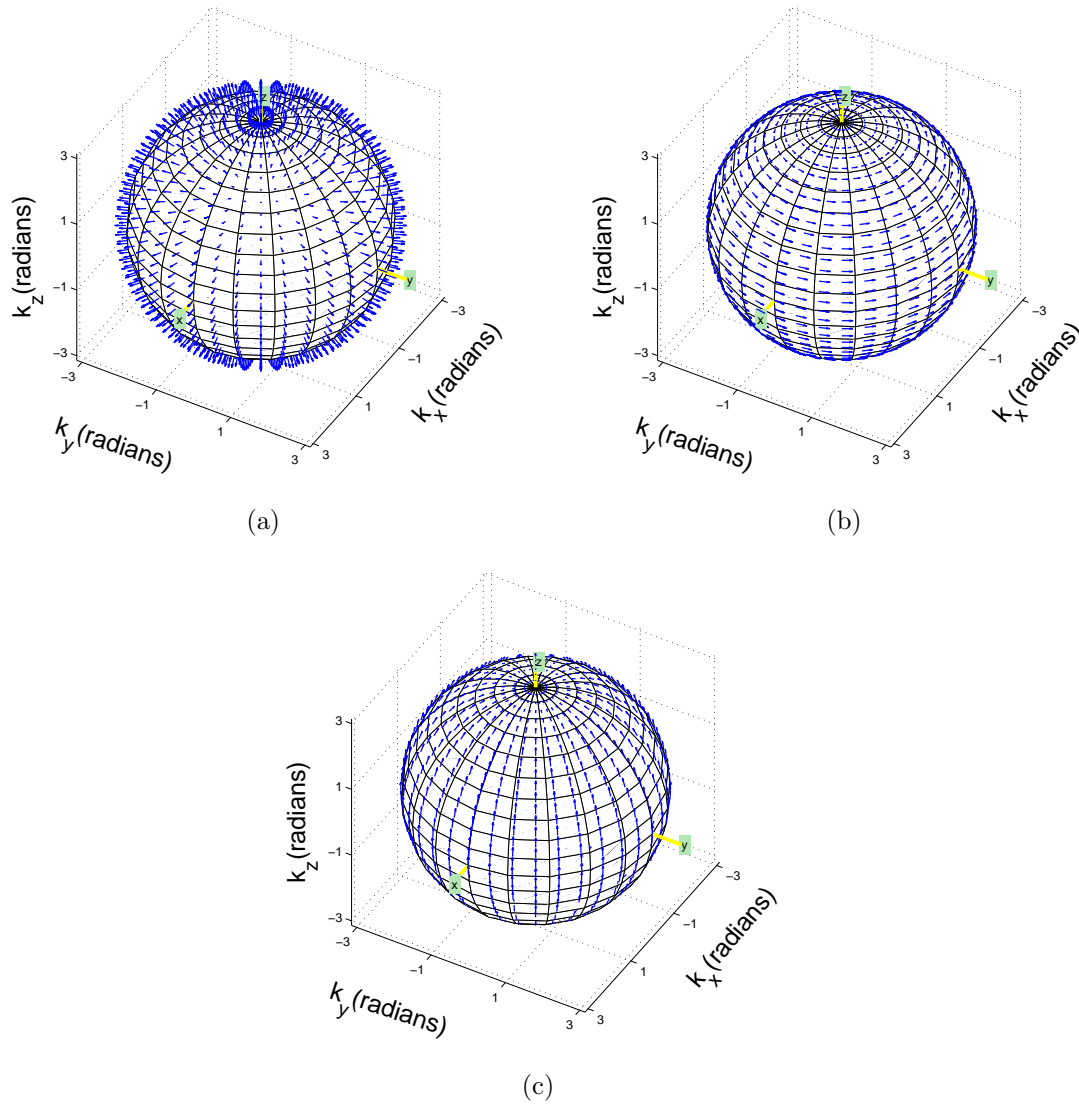


Figure 7: The wave-mode polarization for P-, SH-, and SV-mode for a VTI medium with parameters  $V_{P0} = 4.95$  km/s,  $V_{S0} = 2.48$  km/s,  $\epsilon = 0.4$ , and  $\delta = 0.1$ . The P-mode polarization is computed using the 3D Christoffel equation, and SV and SH polarizations are computed using Equations 21 and 20. Note that the SV- and SH-wave polarization vectors have zero amplitude in the vertical direction.

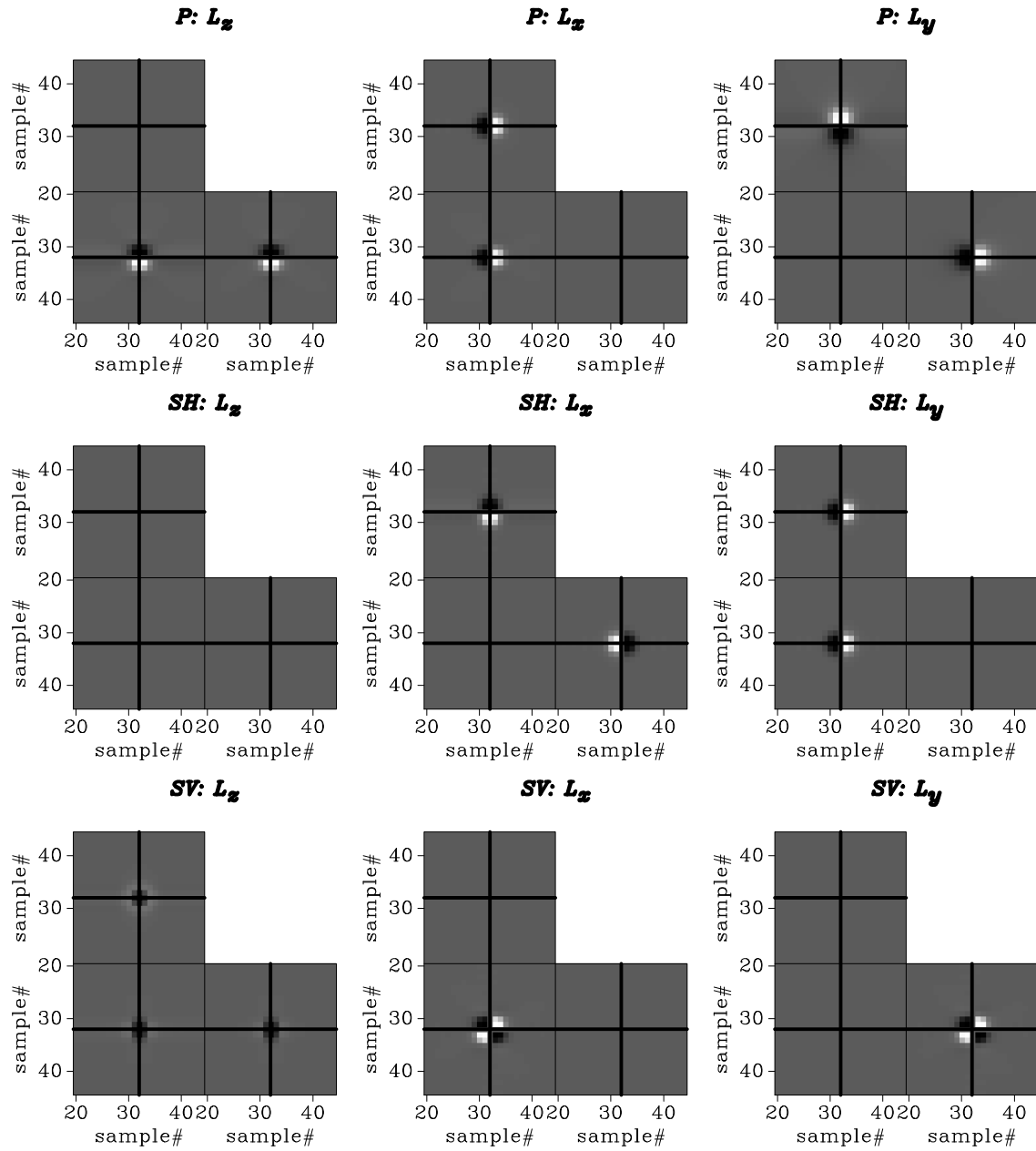


Figure 8: The separation filters  $L_x$ ,  $L_y$ , and  $L_z$  for the P, SV, and SH modes for a VTI medium. The corresponding wavenumber-domain polarization vectors are shown in Figure 7. Note that the filter  $L_z$  for the SH mode is blank because the  $z$  component of the polarization vector is zero. The zoomed views show  $24 \times 24$  samples out of the original  $64 \times 64$  samples around the center of the filters.

## EXAMPLES

I illustrate the anisotropic wave-mode separation with a simple fold synthetic example and a more challenging model based on the elastic Marmousi II model (Bourgeois et al., 1991). I then show the wave-mode separation for a 3D TTI model.

### 2D TTI fold model

Consider the 2D fold model shown in Figure 9. Panels 9(a)–(f) show  $V_{P0}$ ,  $V_{S0}$ , density, parameters  $\epsilon$ ,  $\delta$ , and the local tilts  $\nu$  of the model, respectively. The symmetry axis is orthogonal to the reflectors throughout the model. Figure 10 illustrates the separators obtained at different locations in the model and defined by the intersections of  $x$  coordinates 0.15, 0.3, 0.45 km and  $z$  coordinates 0.15, 0.3, 0.45 km, shown by the dots in Figure 9(f). Since the operators correspond to different combinations of the  $V_{P0}/V_{S0}$  ratio and parameters  $\epsilon$ ,  $\delta$ , and tilt angle  $\nu$ , they have different forms. However, the orientation of the operators conform to the corresponding tilts at the locations shown by the dots in Figure 9(f). For complex models, the symmetry axes vary spatially, which makes it difficult to rotate the wavefields to the local symmetry axis directions. Consequently, the elastic wavefields are reconstructed in untilted Cartesian coordinates, and when separating wave-modes, I use operators constructed in conventional Cartesian coordinates. To illustrate the relationship between the operators and the local tilts, the filters in Figure 10 are projected onto the local symmetry axes and the orthogonal directions at the filter location. As shown in Figure 4, the rotated filters (Figure ??) show a clearer relation with the tilt angle, while the non-rotated filters (Figure ??), which are used in the wave-mode separation, do not show a clear relation with the tilt angle.

Figure 11(a) shows the vertical and horizontal components of one snapshot of the simulated elastic anisotropic wavefield; Figure 11(b) shows the separation into P- and S-modes using divergence and curl operators; Figure 11(c) shows the separation into  $qP$  and  $qS$  modes using VTI filters, i.e., assuming zero tilt throughout the model; and Figure 11(d) shows the separation obtained with the TTI operators constructed using the local medium parameters with correct tilts. The isotropic separation shown in Figure 11(b) is incomplete; for example, at  $x = 0.4$  km and  $z = 0.1$  km, and at  $x = 0.4$  km and  $z = 0.35$  km, residuals for direct P and S arrivals are visible in the  $qP$  and  $qS$  panels, respectively. A comparison of Figures 11(c) and (d) indicates that the spatially-varying derivative operators with correct tilts successfully separate the elastic wavefields into  $qP$  and  $qS$  modes, while the VTI operators only work in the part of the model that is locally VTI.

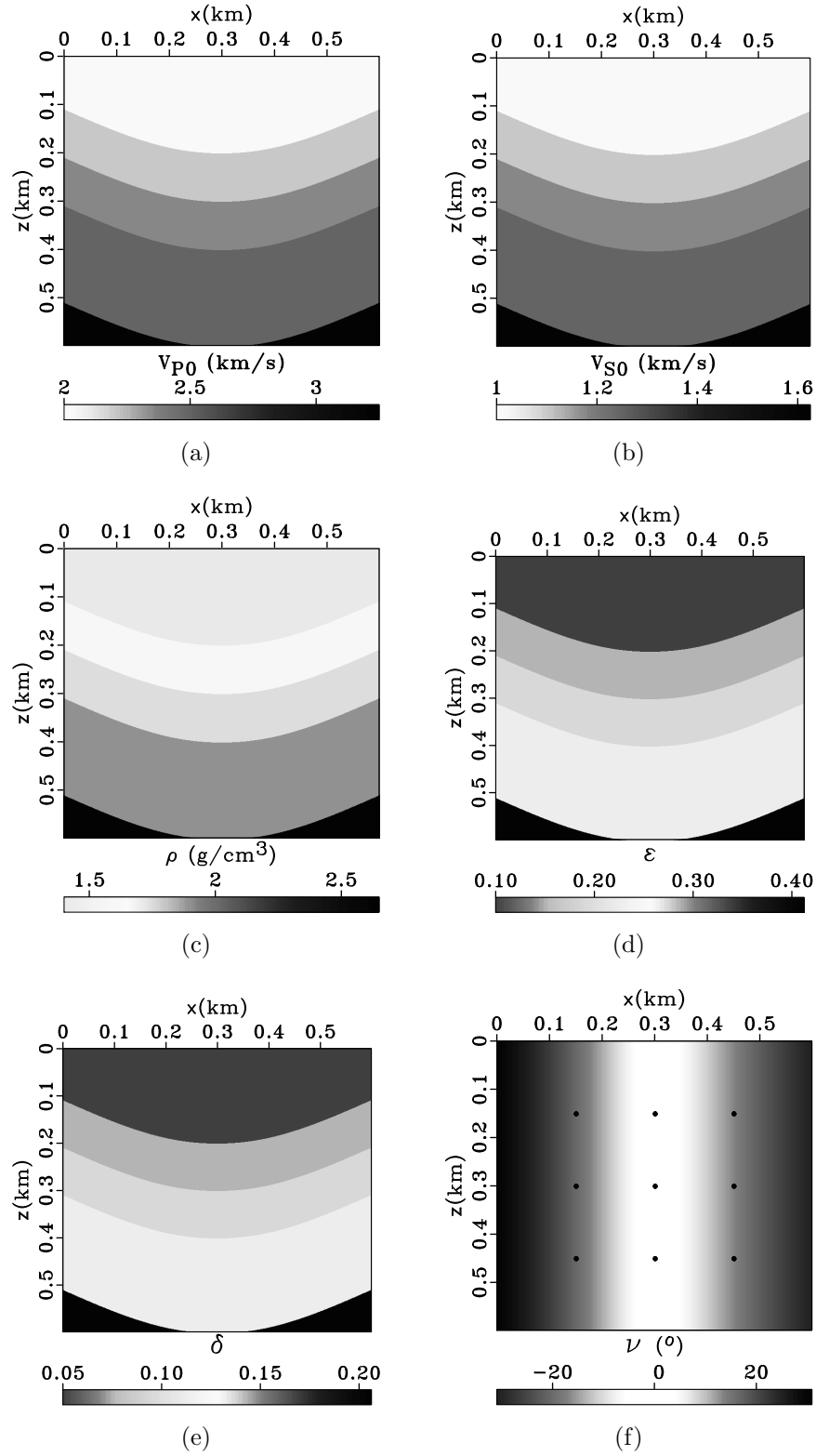


Figure 9: A fold model with parameters (a)  $V_{P0}$ , (b)  $V_{S0}$ , (c) density, (d)  $\epsilon$ , (e)  $\delta$ , and (f) tilt angle  $\nu$ . The dots in panel (f) correspond to the locations of the anisotropic operators shown in Figure 10.

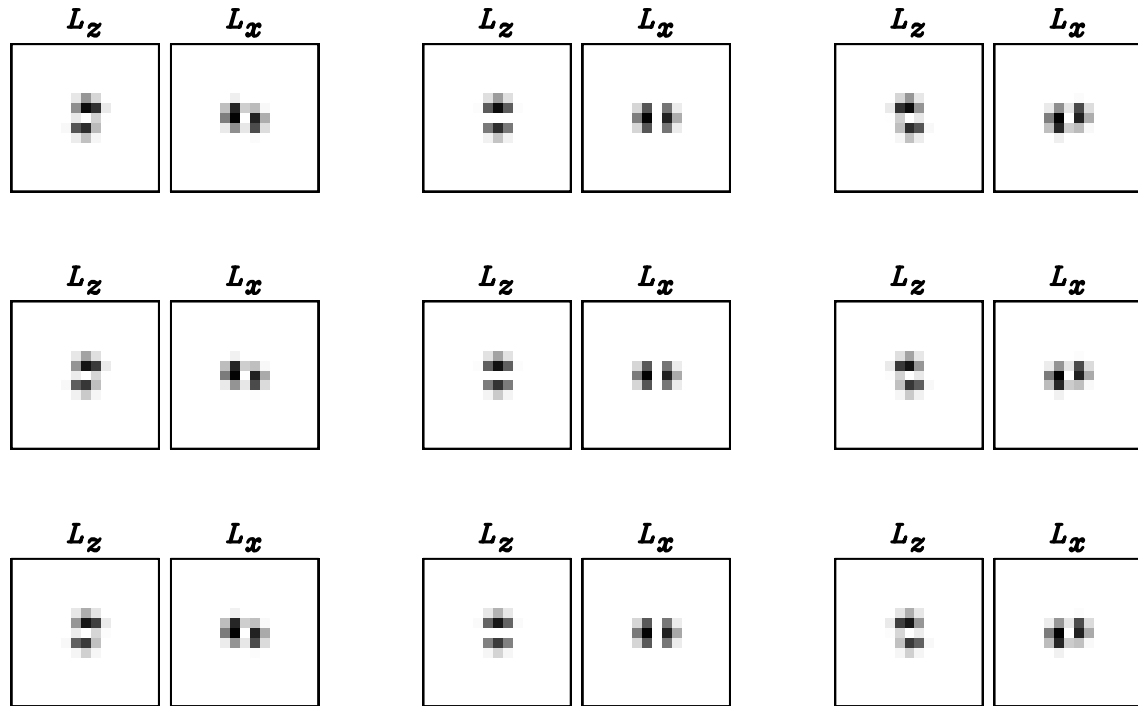


Figure 10: The TTI wave-mode separation filters projected to local symmetry axes and their orthogonal directions. Here, I use  $\sigma = 1$  in equation 12 to taper the polarization vector components before the Fourier transform. The filters correspond to the intersections of  $x = 0.15, 0.3, 0.45$  km and  $z = 0.15, 0.3, 0.45$  km for the model shown in Figure 9. The locations of these operators are also shown by the dots in Figure 9(f).

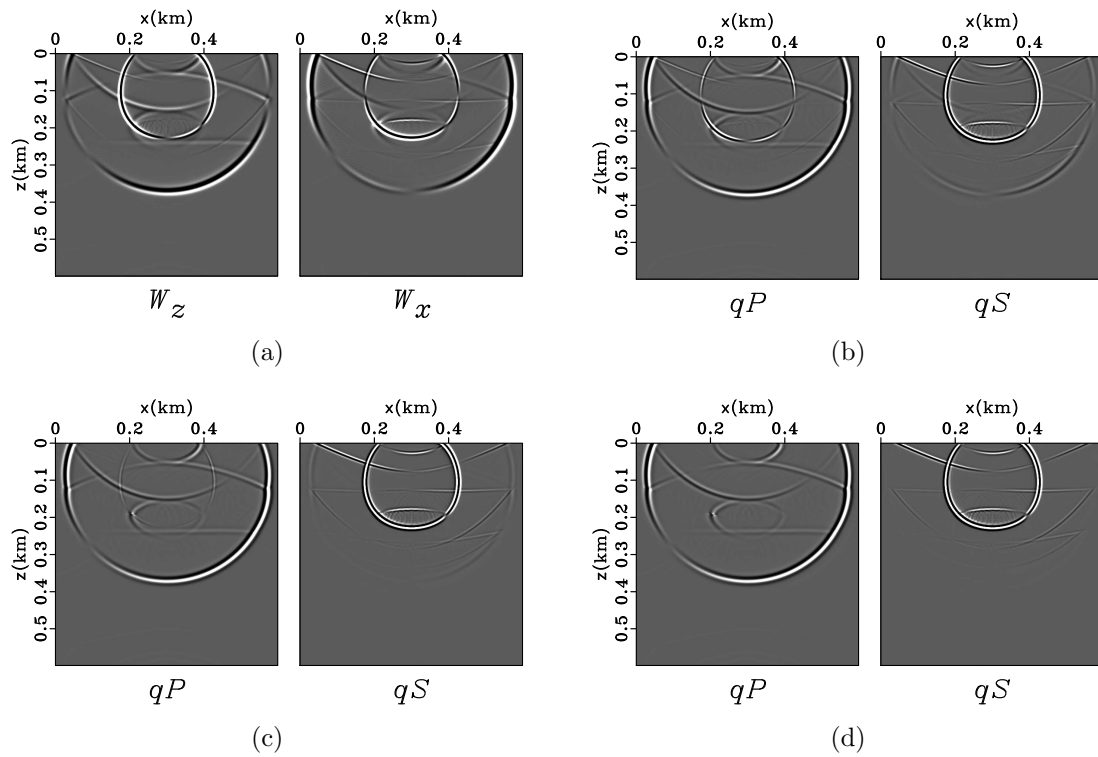


Figure 11: (a) A snapshot of the anisotropic wavefield simulated with a vertical point displacement source at  $x = 0.3$  km and  $z = 0.1$  km for the model shown in Figure 9. Panels (b) to (d) are the anisotropic  $qP$  and  $qS$  modes separated using isotropic, VTI, and TTI separators, respectively. The separation is incomplete in panels (b) and (c) where the model is strongly anisotropic and where the model tilt is large, respectively. Panel (d) shows the best separation among all.

## Marmousi II model

My second model (Figure 12) uses an elastic anisotropic version of the Marmousi II model (Bourgeois et al., 1991). In the modified model,  $V_{P0}$  is taken from the original model (Figure 12(a)), the  $V_{P0}/V_{S0}$  ratio ranges from 2 to 2.5, (Figure 12(b)), and the density  $\rho$  is taken from the original model (Figure 12(c)). The parameter  $\epsilon$  and  $\delta$  are derived from the density model  $\rho$  with the relations of  $\epsilon = 0.25\rho - 0.3$  and  $\delta = 0.125\rho - 0.1$ , respectively. The parameter  $\epsilon$  ranges from 0.13 to 0.36 Figure 12(d), and parameter  $\delta$  ranges from 0.11 to 0.24 Figure 12(e). These anisotropy parameters are obtained by assuming linear relationships to the velocity models, and therefore, they both follow the structure of the model. Figure 12(f) represents the local dips obtained from the density model using plane wave destruction filters (Fomel, 2002). The dip model is used to simulate the wavefields and also used to construct TTI separators. A displacement source oriented at  $45^\circ$  to the vertical direction and located at coordinates  $x = 11$  km and  $z = 1$  km is used to simulate the elastic anisotropic wavefield.

Figure 13(a) presents one snapshot of the simulated elastic wavefields using the anisotropic model shown in Figure 12. Figures 13(b), (c), and (d) demonstrate the separation using conventional divergence and curl operators, VTI filters, and correct TTI filters, respectively. The VTI filters are constructed assuming zero tilt throughout the model, and the TTI filters are constructed with the dips used for modeling. As expected, the conventional divergence and curl operators fail at locations where anisotropy is strong. For example, in Figure 13(b) at coordinates  $x = 12.0$  km and  $z = 1.0$  km strong S-wave residual exists, and at coordinates  $x = 13.0$  km and  $z = 1.5$  km strong P-wave residual exists. VTI separators fail at locations where the dip is large. For example, in Figures 13(c) at coordinates  $x = 10.0$  km and  $z = 1.2$  km, strong S-wave residual exist. However, even for this complicated model, separation using TTI separators is effective at locations where medium parameters change rapidly.

## 3D TTI model

I use a homogeneous TTI model to illustrate the separation of P-, SV-, and SH-modes. The model has parameters  $V_{P0} = 3.5$  km/s,  $V_{S0} = 1.75$  km/s,  $\rho = 2.0$  g/cm<sup>3</sup>,  $\epsilon = 0.4$ ,  $\delta = 0.1$ ,  $\gamma = 0.0$ ,  $\nu = 30^\circ$ , and  $\alpha = 45^\circ$ . Figure 14 shows a snapshot of the elastic wavefields in the  $z$ ,  $x$ , and  $y$  directions. A displacement source located at the center of the model and oriented at tilt  $45^\circ$  and azimuth  $45^\circ$  is used to excite the wavefield. Figure 15 shows successfully separated P-, SV-, and SH-modes. In this model, the parameter  $\gamma$ , which characterizes the anisotropy of SH-mode, is set to zero so that the SH-mode propagation is isotropic. For this homogeneous model, a spherical wavefront in the SH-panel indicates successful separation of SV- and SH-modes.

Because this model is homogeneous, the separation is implemented in the wavenumber domain to reduce computation cost. For heterogeneous models, 3D non-stationary

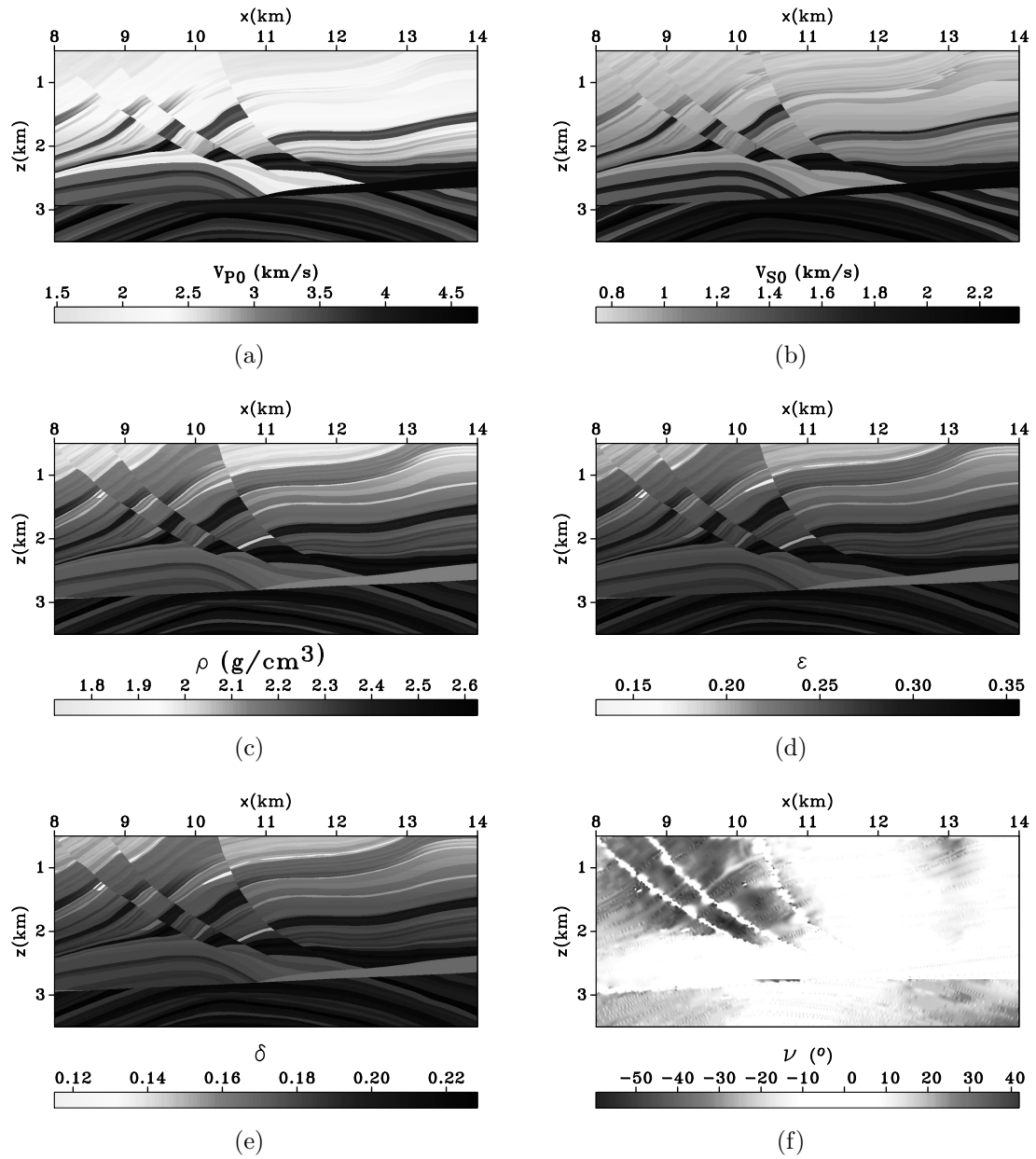


Figure 12: Anisotropic elastic Marmousi II model with (a)  $V_{P0}$ , (b)  $V_{S0}$ , (c) density, (d)  $\epsilon$ , (e)  $\delta$ , and (f) local tilt angle  $\nu$ .

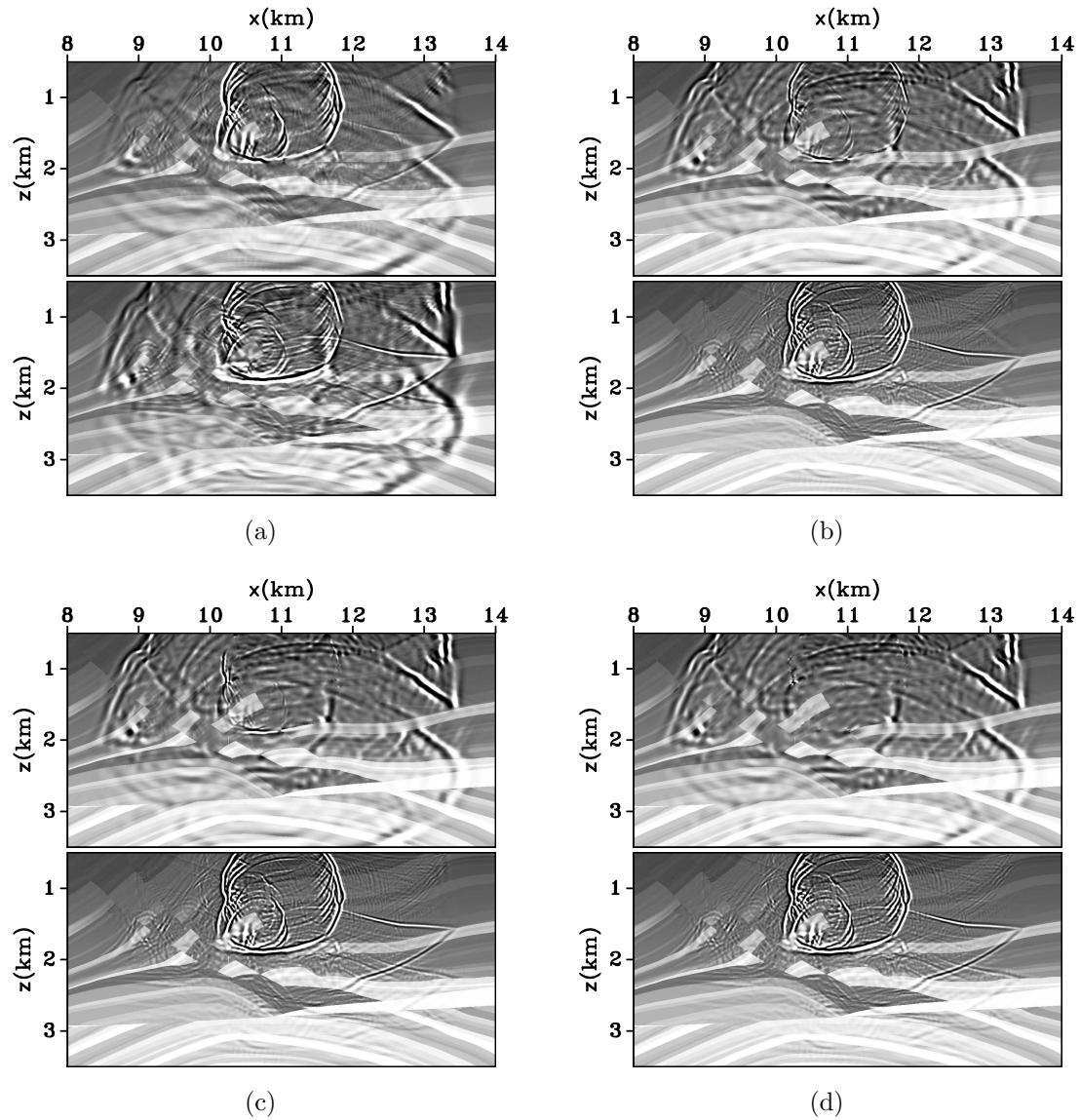


Figure 13: (a) A snapshot of the vertical and horizontal displacement wavefield simulated for model shown in Figure 12. Panels (b) to (c) are the P- and SV-wave separation using  $\nabla \cdot$  and  $\nabla \times$ , VTI separators and TTI separators, respectively. The separation is incomplete in panels (b) and (c) where the model is strongly anisotropic and where the model tilt is large, respectively. Panel (d) shows the best separation among all.

filtering is necessary to separate different wave-modes. I do not perform wave-mode separation in 3D heterogeneous models because of the high computational cost, which will be discussed in more detail in the following section.

## DISCUSSION

### Computational issues

The separation of wave-modes for heterogeneous TI models requires non-stationary spatial filtering with large operators (operators of 50 samples in each dimension are used in this chapter), which is computationally expensive. The cost is directly proportional to the size of the model and to the size of each operator. Furthermore, in a simple implementation, the storage for the separation operators of the entire model is proportional to the size of the model and to the size of each operator. Suppose that a 3D elastic TTI model is characterized by the model parameters  $V_{P0}$ ,  $V_{S0}$ , Thomsen parameters  $\epsilon$  and  $\delta$ , and symmetry axis tilt angle  $\nu$  and azimuth angle  $\alpha$ . For a 3D model of  $300 \times 300 \times 300$  grid points, if one assumes that all operators have a size of  $50 \times 50 \times 50$  samples, the storage for the operators is  $300^3$  grid points  $\times 50^3$  samples/independent operator  $\times 3$  independent operators/grid point  $\times 4$  Bytes/sample = 40.5 TB. This is not feasible in ordinary processing. However, since there are relatively few medium parameters, i.e., the  $V_{P0}/V_{S0}$  ratio,  $\epsilon$ ,  $\delta$ , and angles  $\nu$  and  $\alpha$ , which determine the properties of the operators, one can construct a look-up table of operators as a function of these parameters, and search the appropriate operators at every location in the model when doing wave-mode separation. For example, suppose one knows that  $V_{P0}/V_{S0} \in [1.5, 2.0]$ ,  $\epsilon \in [0, 0.3]$ ,  $\delta \in [0, 0.1]$ , and the symmetry axis tilt angle  $\nu \in [-90^\circ, 90^\circ]$  and azimuth angle  $\alpha \in [-180^\circ, 180^\circ]$ , one can sample the  $V_{P0}/V_{S0}$  ratio at every 0.1,  $\epsilon$  and  $\delta$  at every 0.03, and the angles at every  $15^\circ$ . In this case, one only needs a storage of  $6 \times 10 \times 3 \times 12 \times 24$  combinations of medium parameters  $\times 50^3$  sample/independent operator  $\times 3$  independent operators/combination of medium parameters  $\times 4$  Bytes/sample = 77 GB; this is more manageable, although it is still a large volume to store.

### S wave-mode amplitudes

Although the procedure used in this chapter to separate S-waves into SV- and SH-modes is simple, the amplitudes of S-modes are not accurate because the S-wave separators are not normalized for any given wavenumbers. The amplitudes of S-modes obtained in this way are zero in the symmetry axis direction and they gradually increase to one in the symmetry plane.

The main problem that prevents one from constructing the 3D global shear wave separators is that the SV and SH polarization vectors are singular in the symmetry axis direction, i.e., they are not defined by the plane-wave solution of the TI elas-

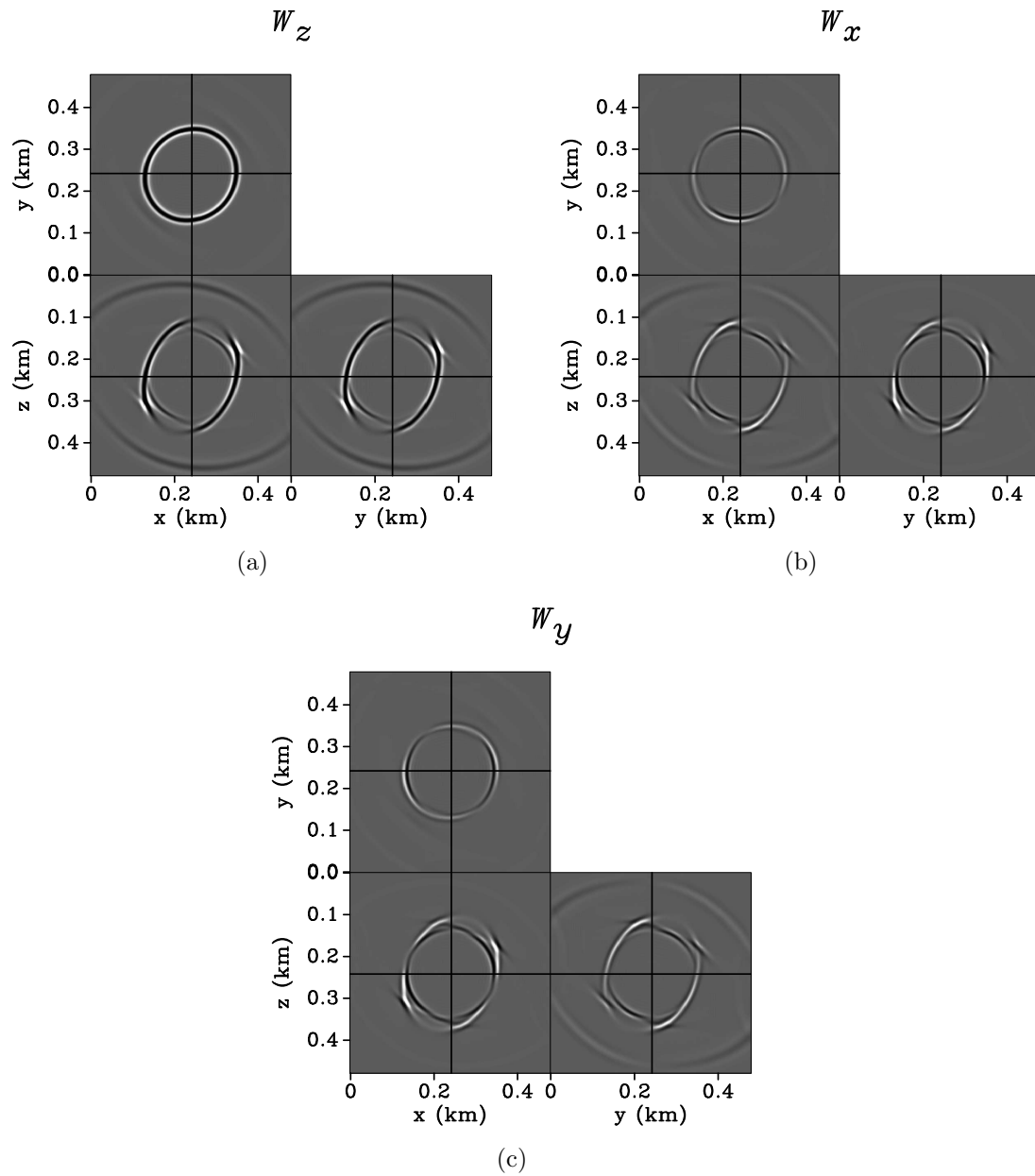


Figure 14: A snapshot of the elastic wavefield in the  $z$ ,  $x$  and  $y$  directions for a 3D VTI model. The model has parameters  $V_{P0} = 3.5$  km/s,  $V_{S0} = 1.75$  km/s,  $\rho = 2.0$  g/cm<sup>3</sup>,  $\epsilon = 0.4$ ,  $\delta = 0.1$ , and  $\gamma = 0.0$ . A displacement source oriented at  $45^\circ$  to the vertical direction and located at coordinates  $x = 11$  km and  $z = 1$  km is used to simulate the elastic anisotropic wavefield.

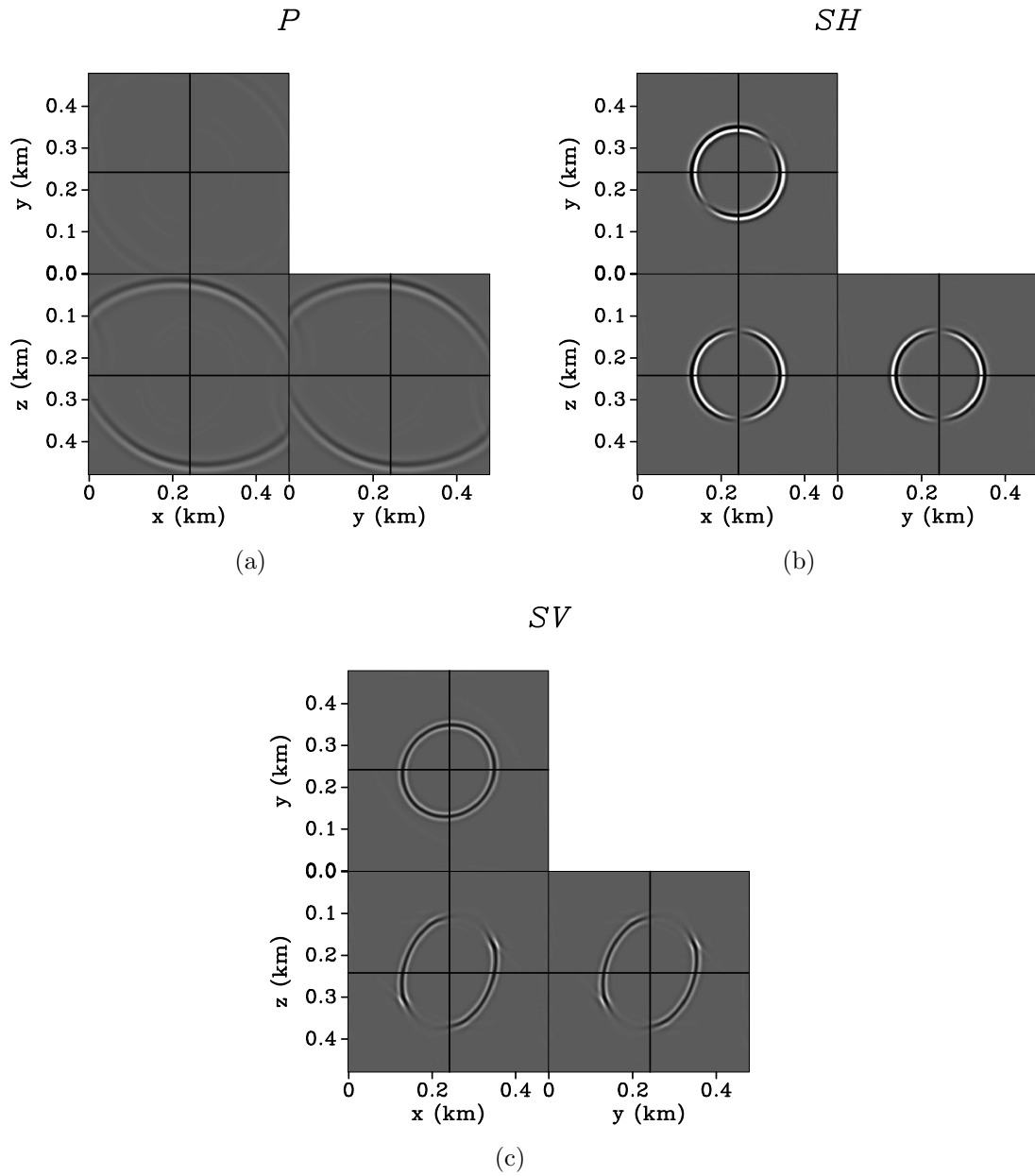


Figure 15: Separated P-, SV- and SH-wave-modes for the elastic wavefields shown in Figure 14. P, SV, and SH are well separated from each other.

tic wave equation. Various studies (Kieslev and Tsvankin, 1989; Tsvankin, 2005) show that S-waves excited by point forces can have non-linear polarizations in several special directions. For example, in the direction of the source, the S-wave can deviate from the linear polarization. This phenomenon exists even in isotropic media. Anisotropic velocity and amplitude variations can also cause the S-waves to be polarized non-linearly. For instance, S-wave triplication, S-wave singularities, and S-wave velocity maximum can all result in S-wave polarization anomalies. In these special directions, SV- and SH-mode polarizations are incorrectly defined by my convention. One possibility for obtaining more accurate S-wave amplitudes is to approximate the anomalous polarization with the major axes of the quasi-ellipses of the S-wave polarization, which can be obtained by incorporating the first-order term in the ray tracing method. This extension remains outside the scope of this chapter.

Although the simplified approach used in this chapter ignores the complicated polarization behavior in some wave propagation directions, it does successfully separate fast and slow shear modes kinematically. This allows one to use the separated scalar shear-modes for the subsequent imaging condition and obtain images with clear physical meaning.

## CONCLUSIONS

Different wave-modes in elastic media can be separated by projecting the vector wavefields onto the polarization vectors of each mode. For heterogeneous models, it is necessary to separate wave-modes in the space domain by non-stationary filtering. I present a method for obtaining spatially-varying wave-mode separators for TI models, which can be used to separate elastic wave-modes in complex media. The method computes the components of the polarization vectors in the wavenumber domain and then transforms them to the space domain to obtain spatially-varying filters. In order for the operators to work in TI models with non-zero tilt angles, I incorporate one more parameter—the local tilt angle  $\nu$ —in addition to the parameters needed for the VTI operators. This kind of spatial filters can be used to separate complicated wavefields in TI models with high heterogeneity and strong anisotropy. I test the separation with synthetic models that have realistic geologic complexity. The results support the effectiveness of wave-mode separation with non-stationary filtering.

I also extend the wave-mode separation to 3D TI models. The P-mode separators can be constructed by solving the Christoffel equation for the P-wave eigenvectors with local medium parameters. The SV and SH separators are constructed using the mutual orthogonality among P, SV, and SH modes. For the three modes, there are a total number of nine separators, with three components for each mode. The separators vary according to the medium parameters  $V_{P0}$ ,  $V_{S0}$ , anisotropy parameters  $\epsilon$  and  $\delta$  and tilt  $\nu$  and azimuth  $\alpha$  of the symmetry axis. The P-wave separators are constructed under no kinematic assumptions, and amplitudes of P-mode correctly characterize the plane-wave solution. Shear wave separators are constructed under kinematic assumptions, and therefore the amplitudes of shear modes are inaccurate

in the singular directions. Nevertheless, the proposed technique successfully separates fast and slow shear wavefields. The process of constructing 3D separators and separating wave-modes in 3D eliminates the step of decomposing the wavefields into symmetry planes, which only works for models with an invariant symmetry axis. Spatially-varying 3D separators have potential benefits for complex models and can be used to separate wave-modes in elastic reverse time migration (RTM) for TTI models. The spatially-varying 3D separators imply large computational and storage cost, and therefore, a more efficient separation method, such as the proposed table look-up alternative, is necessary for a successful implementation.

## ACKNOWLEDGMENT

I acknowledge the financial support of the sponsors of the Center for Wave Phenomena at Colorado School of Mines. The reproducible numeric examples in this paper use the Madagascar open-source software package freely available from <http://www.reproducibility.org>.

## REFERENCES

- Aki, K., and P. Richards, 2002, *Quantitative seismology* (second edition): University Science Books.
- Alkhalifah, T., and P. Sava, 2010, A transversely isotropic medium with a tilted symmetry axis normal to the reflector: *Geophysics*, in press.
- Bourgeois, A., M. Bourget, P. Lailly, M. Poulet, P. Ricarte, and R. Versteeg, 1991, The Marmousi experience, *in* *The Marmousi Experience*, Proceedings of the 1990 EAEG workshop: Marmousi, model and data, 5–16.
- C., S., D. R. Mitchell, R. A. Holt, J. Lin, and J. Mathewson, 2008, Data-driven tomographic velocity analysis in tilted transversely isotropic media: A 3d case history from the canadian foothills: *Geophysics*, **73**, VE261–VE268.
- Dellinger, J., 1991, *Anisotropic seismic wave propagation*: PhD thesis, Stanford University.
- Dellinger, J., and J. Etgen, 1990, Wave-field separation in two-dimensional anisotropic media (short note): *Geophysics*, **55**, 914–919.
- Fomel, S., 2002, Applications of plane-wave destruction filters: *Geophysics*, **67**, 1946–1960.
- Godfrey, R. J., 1991, Imaging Canadian foothills data: 61st Ann. Internat. Mtg, Soc. of Expl. Geophys., 207–209.
- Isaac, J. H., and L. C. Lawyer, 1999, Image mispositioning due to dipping TI media: A physical seismic modeling study: *Geophysics*, **64**, 1230–1238.
- Kieslev, A. P., and I. Tsvankin, 1989, A method of comparison of exact and asymptotic wave field computations: *Geophysical Journal International*, **96**, 253–258.
- Stewart, R. R., J. Gaiser, R. J. Brown, and D. C. Lawton, 2003, Converted-wave seismic exploration: Applications: *Geophysics*, **68**, 40–57.

- Sun, R., G. A. McMechan, H. Hsiao, and J. Chow, 2004, Separating P- and S-waves in prestack 3D elastic seismograms using divergence and curl: *Geophysics*, **69**, 286–297.
- Thomsen, L., 1986, Weak elastic anisotropy: *Geophysics*, **51**, 1954–1966.
- Tsvankin, I., 2005, *Seismic signatures and analysis of reflection data in anisotropic media: 2nd edition*: Elsevier Science Publ. Co., Inc.
- Vestrum, R. W., L. C. Lawyer, and R. Schmid, 1999, Imaging structures below dipping TI media: *Geophysics*, **64**, 1239–1246.
- Yan, J., and P. Sava, 2008, Isotropic angle-domain elastic reverse-time migration: *Geophysics*, **73**, S229–S239.
- , 2009, Elastic wave-mode separation for VTI media: *Geophysics*, **74**, WB19–WB32.